

Temperature dependence of LiNbO_3 dislocation density in the near-surface layer

Oksana Semenova^{1*}, Aleksei Sosunov¹, Nikolai Prokhorov¹, and Roman Ponomarev^{1,2}

¹Department of Nanotechnology and Microsystems Engineering, Perm State University, Perm 614990, Russia

²Perm Federal Research Center of the Ural Branch of the Russian Academy of Sciences, Perm 614990, Russia

*Corresponding author: orsemenova@psu.ru

Received January 24, 2022 | Accepted April 2, 2022 | Posted Online May 4, 2022

Density of dislocations in the near-surface layer was investigated in X -cut LiNbO_3 depending on thermal annealing in the temperature range of 400°C–600°C. A dynamic model of randomly distributed dislocations has been developed for LiNbO_3 by using X-ray diffraction. The experimental results showed that the dislocation density of the near-surface layer reached the minimum at the thermal annealing temperature of 500°C, with the analysis being performed when wet selective etching and X-ray diffraction methods were used. We concluded that homogenization annealing is an effective technique to improve the quality of photonic circuits based on LiNbO_3 . The results obtained are important for optical waveguides, LiNbO_3 -on-insulator-based micro-photonic devices, electro-optical modulators, sensors, etc.

Keywords: lithium niobate; etching pits; near-surface layer; density of dislocations; annealing; X-ray diffraction.

DOI: [10.3788/COL202220.061601](https://doi.org/10.3788/COL202220.061601)

1. Introduction

Lithium niobate (LiNbO_3 , LN) is a well known and commercially available material of great importance for integrated optics—"the silicon of photonics," due to its excellent characteristics: a wide transparency window of 0.35–5.5 μm , high Curie temperature -1145°C , and electro-optical coefficients $r_{33} = 32 \text{ pm/V}$. LN is widely used for the manufacture of LN-on-insulator (LNOI) components^[1], electro-optical modulators^[2], navigation systems^[3], and sensors^[4]. Also, LN is used for novel applications like memristors^[5], photonic integrated circuits (PICs) with ferroelectric domain engineering^[6], direct femtosecond laser micromachining and fast prototyping^[7], and second harmonic generation and metasurface devices^[8,9].

For all these applications, the important role is not of the bulk properties of LN but of its near-surface layer, because the ridge or buried waveguides and electrodes are created on the surface of the crystal. Some authors^[10] describe in detail the various ferroelectric properties of the LN surface and the prospects for its applications. LN is an anisotropic crystal, and each crystallographic edge has its own characteristics. Z -cut LN is of strong interest due to its polar nature, which potentially allows for many different applications. The X -cut is the more technologically relevant surface of LN, being neither polar nor piezoelectric.

It is well known that electro-optical properties of LN are sensitive to the intrinsic defects and impurities. Structure defects in LN crystals can be roughly divided into two types: internal,

related to the crystal growth, and external, related to the wafer dicing and polishing. The defect structure of a congruent LN consists of Li vacancies, Nb_{Li} -antisites, oxygen vacancies, polarons, bound polarons, and bi-polarons^[11]. The crystal structure of the surface for the X -cut shows some deviation in the oxygen sublattice from the ideal template, as marked in Ref. [10].

External or technological defects arise during the cutting and polishing of LN. Despite the high quality of the optical surface, which is obtained during cutting and polishing, the number of defects increases^[12]. The appearance and multiplication of defects occur mainly in the near-surface layer^[13,14]. These defects lead to a significant deviation of $[\text{Li}]/[\text{Nb}]$ -cations ratio and the appearance of more complex forms of structural imperfections, facilitating the diffusion processes^[15]. The amount and quality of such defects are determined by technological parameters of thermal and electrothermal treatment and the dopant and impurity composition of the crystal^[16].

The structure of the damaged near-surface layer in LN has a deformation nature with the multiplication of the dislocation density^[14] and can be described using Bochvar–Oding's curve. Bochvar–Oding's curve describes the dependence of the yield stress on the dislocation density. The number of etching pits on its surface determines the density of dislocations in the near-surface layer of LN. Thus, one of the effective methods for controlling the density of defects and dislocations is the thermal annealing^[17]. In integrated silicon-based technologies, the chemical–mechanical polishing with nanoabrasives is standard

to reduce the damaged surface layer^[18–20], but LN is quite resistant to chemical influences^[21].

The aim of this work is to analyze experimentally and theoretically the dislocation density of the near-surface layer of LN as a function of the thermal annealing temperature.

2. Materials and Methods

The samples used for the investigations were congruent X-cut LN 1-mm-thick wafers by Fomos Materials (Russia). The wafers were cut into 10 mm × 15 mm pieces, where the short side coincided with polar axis *Z* of the crystal.

Thermal annealing (treatment) of LN was performed at temperatures of 400°C, 500°C, and 600°C in air atmosphere. The samples were heated by 10°C/min to the required temperature, then for 4 h they were annealed, and after that they were slowly cooled in the furnace. In addition, there was a reference sample without annealing. Thermal annealing is required to reduce internal stresses, absorption^[22], and damaged near-surface layers of LN. In the selected temperature range, an increase in the homogeneity of the structure of the near-surface layer is observed^[17]; there is no Li loss, and there is no increase in the number of Nb_{Li}-antisite defects and oxygen vacancies^[23].

The dislocation density on the surface of LN was estimated by the method of identifying etching pits by using wet selective etching in the melt of KOH with 35% NaOH for 5 min at a temperature 200°C. Detection of etching pits was carried out using the optical microscope Leica DMI8 in reflected light and a bright field. All samples were cleaned sequentially in isopropyl alcohol and distilled water for 3 min in an ultrasonic bath.

The topology of the etch pits was studied using atomic force microscopy (AFM) in the semi-contact mode (NT-MDT NTEGRA Prima Corp.). Analysis and quantitative calculation of AFM images were carried out using the program Nova 1.1.1 NT-MDT.

The dislocation density was also experimentally estimated using the X-ray method based on the account of an extinction effect in imperfect single crystals, using a model of randomly distributed dislocations. X-ray diffraction (XRD) was carried out by using a precise double-crystal spectrometer. The monochromator was a dislocation-free Si crystal, set in the position corresponding to the reflection K-line of Co-radiation ($\lambda = 1.62075 \text{ \AA}$, $1 \text{ \AA} = 0.1 \text{ nm}$) from the crystallographic plane (111). Integrated intensities were obtained for the first and second orders of the X-ray reflections with indices (110) and (220), respectively. The integral intensity of X-ray peaks was calculated by numerical integration with Simpson's rules.

3. Results

3.1. Wet selective etching

The real structure of LN was revealed by the wet selective etching method, which can be used to analyze the dislocation density. Many etching pits appear on the surface with selective etching,

which are the emergence of dislocations caused by cutting and grinding of a monocrystalline wafer. Also, the authors^[24] showed that the crystal surface can have multidirectional scratches not only after mechanical processing, but even after chemical–mechanical polishing. Etching pits have a certain geometric shape depending on the crystallographic plane. For the X-cut LiNbO₃, the dislocation etching pits have a diamond shape^[25]. It can be seen from Fig. 1 that the etching pits are elongated along a certain direction. This is the crystallographic direction $[01\bar{1}1]$, which corresponds to the prismatic slip system $\{\bar{1}2\bar{1}0\}/(\bar{1}101)$ in LN. Note that the shape of the etching pits for various samples is highly distorted rhombuses, in some cases elongated along one of the diagonals. The distortion of the rhombus shape is a consequence of microdeformations of the near-surface layer of the LN crystal; the stronger the distortion, the greater the deviation of the etched plane from the $(\bar{2}110)$ plane.

The near-surface layer of the crystal was treated by thermal annealing to reduce the density of dislocations and stresses. The dislocation etching pits on the surface before and after thermal annealing were detected with an optical microscope (Fig. 1). The calculated dislocation density *N* is presented in Fig. 2 for treated and reference samples. Each point is the result of

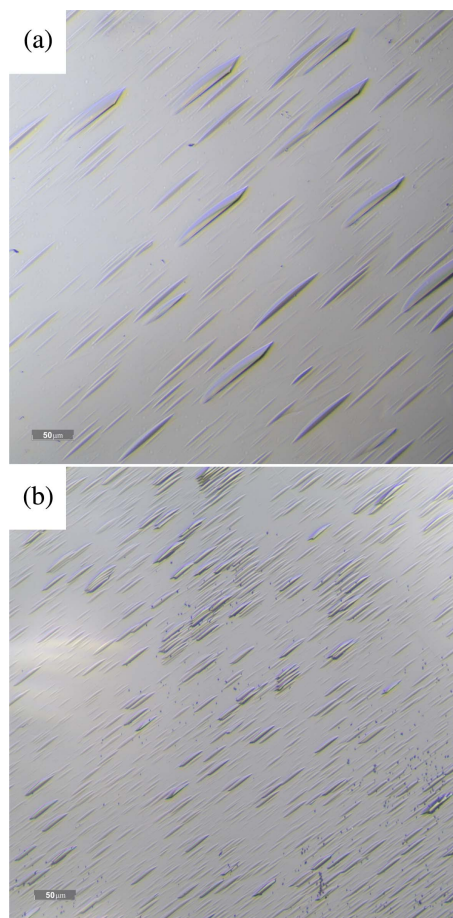


Fig. 1. Etching pits of LiNbO₃ (a) after thermal annealing at 500°C and (b) in pristine state.

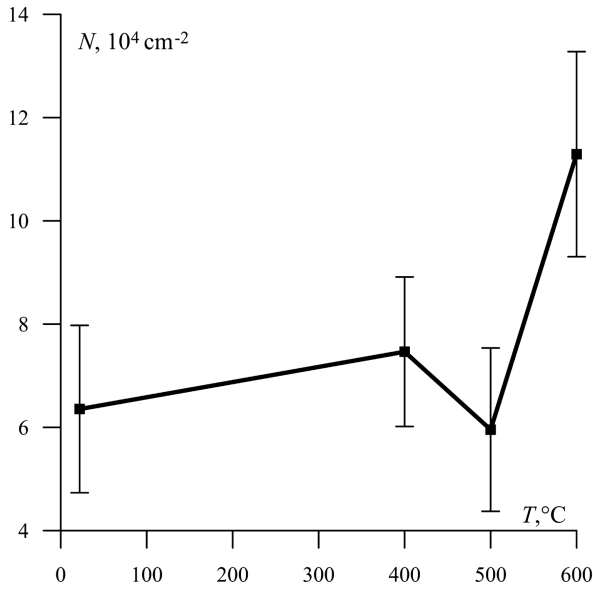


Fig. 2. Dependence of the dislocation density N determined by wet selective etching on the annealing temperature T .

averaging 10 sections of the wafer. Etching pits were counted manually due to the low contrast of transparent materials and many artifacts.

For determination of the etching depth some samples were studied using AFM. The distribution profiles of the pits by their depth were obtained. One of these profiles is shown in Fig. 3. The etching pit depth varies from 5 to 100 nm. This means that the etching rate is from 1 to 20 nm/min.

3.2. X-ray diffraction results: theory and experiment

When considering XRD on single crystals, it is necessary to take into account the dynamic extinction effects, which lead to a decrease in the integral reflection coefficients ρ_{HKL} of X-rays in comparison with the calculation of a kinematic theory^[26]. The extinction parameter

$$y_{HKL} = \frac{\rho_{HKL}}{\rho_{HKL}^{\text{kin}}} \leq 1, \quad (1)$$

where ρ_{HKL} is the integral reflection coefficient obtained in the experiment; ρ_{HKL}^{kin} is the integral reflection coefficient calculated using the kinematic theory.

The value of y_{HKL} depends on the type of distribution and density of defects of the crystal structure. In the case of a chaotic distribution of dislocations in a single crystal, the extinction effect is related to the fact that there is a strongly distorted region of the crystal around each dislocation, scattering in accordance to the kinematic theory. The remaining volume of the crystal scatters X-rays according to the dynamic theory. Kinematic volumes can be represented as straight circular cylinders of radius r , drawn around each dislocation line.

The radiation scattered by kinematic volumes is incoherent among instances and with the radiation scattered by the rest

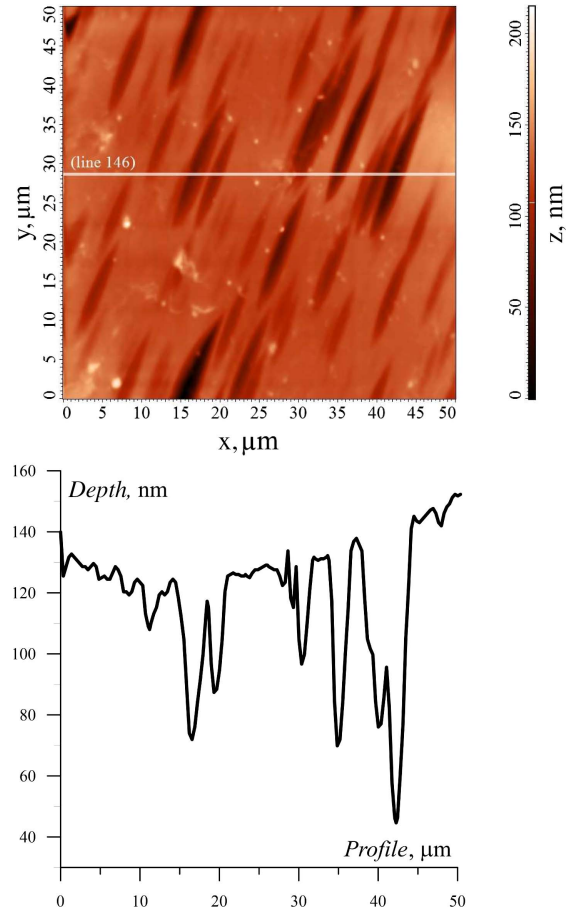


Fig. 3. AFM image of etch pits and the profile of etching pits (line 146).

of the (dynamic) crystal. Then, the integral component of the reflection of the crystal volume is equal to

$$\rho_{HKL} = \rho_{HKL}^{\text{kin}} V_K + \rho_{HKL}^{\text{dyn}} (1 - V_K), \quad (2)$$

where V_K is the fraction of the volume occupied by kinematic regions; ρ_{HKL}^{kin} and ρ_{HKL}^{dyn} are the integral reflection components according to the kinematic and dynamic scattering theory, respectively.

Considering the two types of polarization $\sigma - (\perp)$ and $\pi - (\parallel)$ ^[26], when non-polarized or partially polarized radiation falls on the crystal, the integral reflection coefficient is equal to

$$\rho_{HKL} = \rho_{\perp HKL} + \rho_{\parallel HKL}.$$

Here, $\rho_{\parallel HKL} = \rho_{\perp HKL} B$, where $B = \cos^2 2\theta \cos^2 2\alpha$ is a parameter that accounts for the polarization of radiation when reflected from a monochromator crystal at an angle α ; θ is the Bragg's angle corresponding to reflection (HKL). For both types of components of the integral reflection coefficient according to the kinematic and dynamic scattering theory taking into account Eq. (2), we have

$$\begin{aligned}\rho_{\perp HKL} &= \rho_{\perp HKL}^{\text{kin}} V_{\perp K} + \rho_{\perp HKL}^{\text{dyn}} (1 - V_{\perp K}), \\ \rho_{\parallel HKL} &= \rho_{\parallel HKL}^{\text{kin}} V_{\parallel K} + \rho_{\parallel HKL}^{\text{dyn}} (1 - V_{\parallel K}).\end{aligned}$$

Therefore, an integral reflection coefficient and an extinction parameter are equal to

$$\begin{aligned}\rho_{HKL} &= \frac{\rho_{HKL}^{\text{kin}} \{ [V_{\perp K} + A_{\perp} (1 - V_{\perp K})] + B [V_{\parallel K} + A_{\parallel} (1 - V_{\parallel K})] \}}{1 + B},\end{aligned}\quad (3)$$

and

$$\gamma_{HKL} = \frac{[V_{\perp K} + A_{\perp} (1 - V_{\perp K})] + B [V_{\parallel K} + A_{\parallel} (1 - V_{\parallel K})]}{1 + B}, \quad (4)$$

respectively. Here, $A_{\perp} = \rho_{\perp HKL}^{\text{dyn}} / \rho_{\perp HKL}^{\text{kin}}$ and $A_{\parallel} = \rho_{\parallel HKL}^{\text{dyn}} / \rho_{\parallel HKL}^{\text{kin}}$. The value of A can be found as^[26]

$$A = \frac{1}{2} \mu \frac{t_0}{\sin \theta} \left(1 - \frac{3}{8} \mu \frac{t_0}{\sin \theta} \right), \quad (5)$$

where t_0 is the extinction depth, and μ is the mass absorption coefficient of the crystal.

In the case of Bragg's angle, the extinction depth is^[26]

$$t_0 = \frac{\pi V_0}{r_0 \lambda C \text{Re } F_{HKL}} \sin \theta. \quad (6)$$

Here, $\lambda = 1.62075 \text{ \AA}$ is the wavelength of X-ray; V_0 is the volume of the unit cell of LN; $r_0 = 2.82 \times 10^{-13} \text{ cm}$ is the classical radius of the electron; C is a multiplier taking the value of one for σ polarization (\perp) and $|\cos 2\theta|$ for π -polarization (\parallel); $\text{Re } F_{HKL}$ is the real part of the structural amplitude of LN.

The part of the kinematic volume V_K at the dislocation density N is equal to^[27]

$$V_K = 1 - e^{-NGS_{\sigma,\pi}}, \quad (7)$$

where G is the weight factor, which is equal to the fraction of dislocations satisfying the condition $\mathbf{g}\mathbf{b} \neq 0$, since at $\mathbf{g}\mathbf{b} = 0$ the radius $r = 0$, i.e., this dislocation does not have a kinematic region with respect to the reflex (HKL) [$\mathbf{g} = H\mathbf{a}^* + K\mathbf{b}^* + L\mathbf{c}^*$ is the radius vector of the inverse lattice node (HKL), \mathbf{b} is the Burgers vector of the dislocation], $S_{\sigma,\pi}$ is the scattering area, which is determined as

$$S_{\sigma,\pi} = \pi r^2 = t_0^2 \mathbf{g}\mathbf{b} / \pi. \quad (8)$$

For X-cut samples, the observation plane of etching pits ($\bar{2}110$) is a prismatic sliding plane. It is equivalent from the point of view of symmetry to the planes ($11\bar{2}0$) and ($1\bar{2}10$). X-cut planes in LN correspond to the directions of dislocation lines $[10\bar{1}1]$ and $[10\bar{1}0]$. Note that the dislocation with the Burgers vector $\frac{1}{3}[10\bar{1}1]$ is a partial dislocation from the full dislocation with

the Burgers vector $\frac{1}{3}[2\bar{1}\bar{1}0]$, which was considered in Ref. [28] when studying small-angle boundaries in single crystals of LN:

$$\frac{1}{3}[2\bar{1}\bar{1}0] = \frac{1}{3}[1\bar{1}00] + \frac{1}{3}[10\bar{1}0]. \quad (9)$$

These Burgers vectors are located on the basis plane (0111), i.e., it should be considered for a Z-cut. Therefore, we will consider the sliding directions $[10\bar{1}1]$ and $[10\bar{1}0]$.

Calculating the weight factor G for the considered directions in the X-cut plane gives a value of 2/3 for reflections (110) and (220).

An expression of the integral reflection coefficients ρ_{110}/ρ_{220} , corresponding to two different reflection orders, in terms of the dislocation density is obtained:

$$\begin{aligned}\frac{\rho_{110}}{\rho_{220}} &= \frac{\rho_{H_1K_1L_1}^{\text{kin}}}{\rho_{H_2K_2L_2}^{\text{kin}}} \cdot \frac{1 + B_2}{1 + B_1} \\ &\times \frac{[V_{\perp K}^{(1)} + A_{\perp}^{(1)}(1 - V_{\perp K}^{(1)})] + B_1[V_{\parallel K}^{(1)} + A_{\parallel}^{(1)}(1 - V_{\parallel K}^{(1)})]}{[V_{\perp K}^{(2)} + A_{\perp}^{(2)}(1 - V_{\perp K}^{(2)})] + B_2[V_{\parallel K}^{(2)} + A_{\parallel}^{(2)}(1 - V_{\parallel K}^{(2)})]}.\end{aligned}\quad (10)$$

Here, the index "(1)" refers to the first-order reflections (110), and the index "(2)" refers to the second-order reflections (220), $B_1 = \cos^2 2\theta_1 \cos^2 2\alpha$, and $B_2 = \cos^2 2\theta_2 \cos^2 2\alpha$.

Equation (10) allows us to construct a theoretical dependence of the ratio of the integral reflection coefficients corresponding to two reflection orders to the density of chaotically distributed dislocations, shown in Fig. 4. To determine the density of dislocations in single crystals, the left branch of the presented curve should be used. That is because LN is a brittle material in which it is impossible to create conditions corresponding to large dislocation densities during plastic deformation.

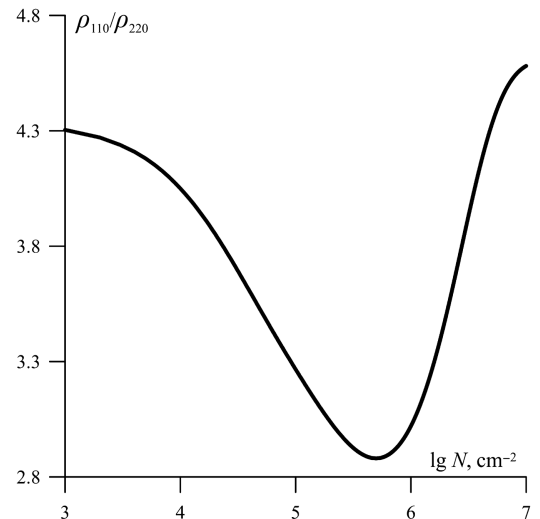


Fig. 4. Dependence of ρ_{110}/ρ_{220} for a single crystal of X-cut LN on the density of chaotically distributed dislocations N , X-ray Co- λ_{β} -radiation.

Table 1. The Experimental Ratio of the Integral Reflection Coefficients ρ_{110}/ρ_{220} .

Thermal Annealing	Sample ρ_{110}/ρ_{220}
Pristine	3.17
400°C – 4 h	3.26
500°C – 4 h	3.57
600°C – 4 h	3.55

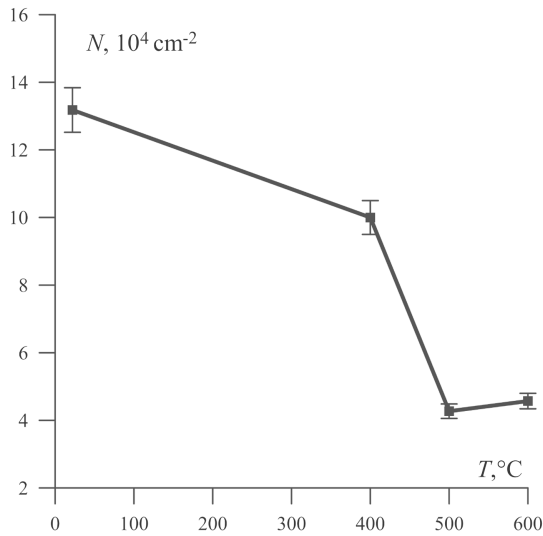
**Fig. 5.** Dependence of the dislocation density N (determined by the results of XRD) on the thermal annealing temperature T .

Table 1 shows the results of measuring the ratio of integral reflection coefficients corresponding to two reflection orders for the studied samples of different manufacturers. Using the results shown in Table 1 and the calculated curve $\rho_{110}/\rho_{220}(N)$ in Fig. 4, the dislocation density for the studied samples was determined. The dependence of dislocation density on treatment temperature is shown in Fig. 5.

4. Discussion

Dislocations characterize the imperfect structure of materials. In this paper, we present results of dislocation density measurement in LiNbO_3 crystal as a function of thermal annealing.

It is known that etching pits do not cover all surface areas of the wafer, but are located in positions where dislocations appear^[29]. The number of pits should not depend on etching time. If etching time increases, then the size of pits increases too, but not the shape. Thus, pits could overlap, and then counting them becomes very difficult. If etching time is not long enough, then we will not see all pits, but only those that are capable of being viewed in an optical microscope. That is why

it initially took a long time to select optimal etching times for reference samples.

Figure 1 shows the decrease in the density of etching pits for treated samples and an increase in their size at a temperature of 500°C. These pictures were chosen because the thermal annealing temperature of 500°C is the most optimal and demonstrates minimum density of etching pits (see Fig. 2). The increase in linear size of etching pits in Fig. 1(a) can be explained by the duration of etching. But, the experimental conditions had to be identical. The etching pits were not ranked by size while being counted. The number of pieces per unit area was counted directly.

LiNbO_3 is a material with a low dislocation density 10^3 – 10^5 cm^{-2} . Our results agree in the order of magnitude with literature data. At a temperature of 400°C, the number of etching pits on the surface of LN increases. This can be explained by the existence of damaged near-surface layers in LN^[17]. Thermal annealing of materials is carried out to relieve microstresses and homogenize the structure. These take place via the increased mobility of the particles forming the crystal lattice due to their increased thermal motion. During annealing, lattice defects otherwise spread in the volume of the material tend to emerge on its surface. It was noted in Ref. [17] that pre-annealing of LN at temperatures of about 500°C makes it possible to reduce the thickness of the damaged near-surface layer. This is consistent with the results obtained in this work (see Fig. 2); upon thermal annealing at 500°C, the dislocation density becomes noticeably lower than at the temperature of 400°C and less compared to reference samples.

A slight increase in the number of defects at 600°C (Fig. 5) indicates the beginning of deformation processes associated with the restructuring of the LN crystal lattice due to the high mobility of the ions at high temperatures. The X-ray method for determining the dislocation density is based on the measurement of integral intensity of the reflection lines of two orders. It is known that the integral intensity is affected by any change in the crystal structure^[26]. At 600°C, the microdeformations of the crystal lattice increase due to its rearrangement. This leads to an increase in the integral intensity of the diffraction line (220), since the microdeformations of the lattice have a greater effect on the integral width of the lines with a large reflection order. Thus, the effect of the microdeformations blurring of the diffraction line causes the differences in the values of N measured by the two methods (Figs. 2 and 5).

Note that etching of single crystals makes it possible to estimate the density of defects on the surface of studied images, and the second method using the X-ray allows the estimation of the density of dislocations to be distributed over the depth of the samples. The volume was determined by the penetration depth of the X-rays. In our case, this was of the order of 15 μm , which is approximately equal to the depth of the defect layer, as reported earlier^[17]. For this reason, the X-ray method used makes it possible to determine a larger number of dislocations, including those that do not have exits to the surface. The results of X-ray analysis (Fig. 5) are in good qualitative agreement with the results of wet selective etching of LN wafers (Fig. 2). The

thermal annealing temperature of 500°C also corresponds to the minimum dislocation density in the near-surface layer in Figs. 2 and 5.

In addition, we note that the proposed extinction model of crystals with random dislocation distribution allows us to measure dislocation density ranging from 10^3 to 10^8 cm⁻². For large dislocation densities (more than 10^8 cm⁻²), we usually use the methods based on the analysis of the physical broadening of XRD lines^[26,27].

Thus, the treatment of LN crystals repairs the damaged layer by reducing the density of dislocations. These results are most important from the point of view of increasing the homogeneity of the structure of the near-surface layer and formation of more stable optical waveguides, integrated-optical circuits, and LNOI components/devices. For example, the creation of ridge waveguides for LNOI is performed by diamond blade dicing with subsequent polishing^[30]. The proposed technique could improve the quality and optical properties of such structures.

5. Conclusion

This work is dedicated to the study of the dislocation density of the near-surface layer of X-cut LN crystals, depending on thermal annealing in the range of 400°C–600°C.

Firstly, the experimental method of wet selective etching was applied to determine the dislocation structure of LN before and after treatment. Secondly, a method was proposed to determine the dislocation density by using XRD based on the account of the extinction effect in imperfect single crystals, using a model of randomly distributed dislocations (theory and experiment). These two methods were used to analyze the dislocation structure of crystals. This is enough to establish a relation between the treatment and the real structure of the LN crystal. It has been experimentally proved that thermal annealing of LN samples at a temperature of 500°C is accompanied by a decrease in the density of dislocations in the near-surface layer.

The obtained results are applicable to other optical materials as well. In addition, the found LN treatment regimen can improve the properties of Ti-diffused, proton-exchanged, and ridge waveguides for various optical systems.

Acknowledgement

The research was funded by state assignment No. 1211013 00016-2.

References

1. A. Boes, B. Corcoran, L. Chang, J. Bowers, and A. Mitchell, "Status and potential of lithium niobate on insulator (LNOI) for photonic integrated circuits," *Laser Photonics Rev.* **12**, 1700256 (2018).
2. K. Noguchi, *Broadband Optical Modulators: Science, Technology, and Applications* (CRC Press, 2012).
3. M. N. Armenise, C. Ciminelli, F. Dell'Olio, and V. M. N. Passaro, *Advances in Gyroscope Technologies* (Springer, 2011).
4. A. V. Turutin, J. V. Vidal, I. V. Kubasov, A. M. Kislyuk, D. A. Kiselev, M. D. Malinkovich, Y. N. Parkhomenko, S. P. Kobeleva, A. L. Kholkin, and N. A. Sobolev, "Highly sensitive magnetic field sensor based on a met-glas/bidomain lithium niobate composite shaped in form of a tuning fork," *J. Magn. Magn. Mater.* **486**, 165209 (2019).
5. P. Chaudhary, H. Lu, A. Lipatov, Z. Ahmadi, J. P. V. McConville, A. Sokolov, J. E. Shield, A. Sinitskii, J. M. Gregg, and A. Gruverman, "Low-voltage domain-wall LiNbO₃ memristors," *Nano Lett.* **20**, 5873 (2020).
6. D. Sun, Y. Zhang, D. Wang, W. Song, X. Liu, J. Pang, D. Geng, Y. Sang, and H. Liu, "Microstructure and domain engineering of lithium niobate crystal films for integrated photonic applications," *Light Sci. Appl.* **9**, 197 (2020).
7. B. Zhang, L. Wang, and F. Chen, "Recent advances in femtosecond laser processing of LiNbO₃ crystals for photonic applications," *Laser Photonics Rev.* **14**, 1900407 (2020).
8. L. Carletti, A. Zilli, F. Moia, A. Toma, M. Finazzi, C. Angelis, D. N. Neshev, and M. Celebrano, "Steering and encoding the polarization of the second harmonic in the visible with a monolithic LiNbO₃ metasurface," *ACS Photonics* **8**, 731 (2021).
9. W. Lu, Z. Gao, X. Liu, X. Tian, Q. Wu, C. Li, Y. Sun, Y. Liu, and X. Tao, "Rational design of a LiNbO₃-like nonlinear optical crystal, Li₂ZrTeO₆, with high laser-damage threshold and wide mid-IR transparency window," *J. Am. Chem. Soc.* **140**, 13089 (2018).
10. S. Sanna and G. Schmidt, "LiNbO₃ surfaces from a microscopic perspective," *J. Phys. Condens. Matter.* **29**, 413001 (2017).
11. R. Bhatt, I. Bhaumik, S. Ganesamoorthy, R. Bright, M. Soharab, A. K. Karnal, and P. K. Gupta, "Control of intrinsic defects in lithium niobate single crystal for optoelectronic applications," *Crystals* **7**, 23 (2017).
12. P. Galinetto, M. Marinone, D. Grando, G. Samoggia, F. Caccavale, A. Morbiato, and M. Musolino, "Micro-Raman analysis on LiNbO₃ substrates and surfaces: compositional homogeneity and effects of etching and polishing processes on structural properties," *Opt. Lasers Eng.* **45**, 380 (2007).
13. M. Gruber, A. Leitner, D. Kiener, P. Supancic, and R. Bermejo, "Incipient plasticity and surface damage in LiTaO₃ and LiNbO₃ single crystals," *Mater. Des.* **153**, 221 (2018).
14. A. V. Sosunov, A. B. Volyntsev, K. B. Tsiberkin, V. A. Yuriev, and R. S. Ponomarev, "Features of structure and mechanical properties LiNbO₃," *Ferroelectrics* **506**, 24 (2017).
15. J. Piecha, A. Molak, U. Breuer, M. Balski, and K. Szot, "Features of surface layer of LiNbO₃ as-received single crystals: studied in situ on treatment samples modified by elevated temperature," *Solid State Ion.* **290**, 31 (2016).
16. A. A. Anikiev, N. V. Sidorov, M. N. Palatnikov, M. F. Umarov, and E. N. Anikieva, "Parametrization of nonstoichiometric lithium niobate crystals with different states of defectivity," *Opt. Mater.* **111**, 110729 (2021).
17. A. Sosunov, R. Ponomarev, O. Semenova, I. Petukhov, and A. Volyntsev, "Effect of pre-annealing of lithium niobate on the structure and optical characteristics of proton-exchanged waveguides," *Opt. Mater.* **88**, 176 (2019).
18. Ya. A. Kosenok, V. E. Gaishun, O. I. Tyulenikova, and V. G. Denisman, "Aqueous compositions based on nanosized silica particles for chemical-mechanical polishing of silicon wafers," *PFMT* **3**, 26 (2014).
19. Y. Li, J. Lu, and X. Xu, "Phase transformation of monocrystalline silicon induced by polishing with diamond abrasives," *IEEE Trans. Semicon. Manuf.* **28**, 153 (2015).
20. Ya. A. Kosenok, V. E. Gaishun, and O. I. Tyulenikova, "Investigation of the near-surface damaged layer in monocrystalline silicon wafers after chemical-mechanical polishing," *PFMT* **4**, 25 (2018).
21. Y. Li, T. Lan, D. Yang, M. Xiang, J. Dai, Z. Wang, and C. Li, "Research of selective etching in LiNbO₃ using proton-exchanged wet etching technique," *Mater. Res. Express* **7**, 056202 (2020).
22. M. Leidinger, K. Buse, and I. Breunig, "Influence of dry-oxygen-annealing on the residual absorption of lithium niobate crystals in the spectral range from 500 to 2900 nanometers," *Opt. Mater. Express* **6**, 264 (2016).
23. T. Volk and M. Wohlecke, *Lithium Niobate: Defects, Photorefractive and Ferroelectric Switching* (Springer, 2008).
24. Z. W. Zhong, "Recent advances in polishing of advanced materials," *Mater. Manuf. Process.* **23**, 449 (2008).
25. K. Nassau, H. J. Levinstein, and G. M. Loiacono, "Ferroelectric lithium niobate. 1. Growth, domain structure, dislocations and etching," *J. Phys. Chem. Solids* **27**, 983 (1966).

26. Z. G. Pinsker, *Dynamical Scattering of X-Rays in Crystals* (Springer-Verlag, 1978).
27. A. N. Ivanov, P. Klimanek, and A. M. Polyakov, "Extinction study of dislocations (Bragg diffraction)," *Mater. Sci. Forum* **321–324**, 87 (2000).
28. A. Nakamura, J. Nakamura, I. Kishida, and Y. Yokogawa, "Dislocation structure at a $\{1\bar{2}10\}/(10\bar{1}0)$ low-angle tilt grain boundary in LiNbO_3 ," *J. Mater. Sci.* **47**, 5086 (2012).
29. K. Sangval, *Etching of Crystals: Theory, Experiment, and Application* (Elsevier Science, 1987).
30. J. Zhao, X. Jiao, Y. Ren, J. Gu, S. Wang, M. Bu, and L. Wang, "Lithium niobate planar and ridge waveguides fabricated by 3 MeV oxygen ion implantation and precise diamond dicing," *Chin. Opt. Lett.* **19**, 060009 (2021).